# Thermal conductivity changes across a structural phase transition: The case of high-pressure silica

Hugo Aramberri,[1] Riccardo Rurali,[1] and Jorge Íñiguez[2]

[1]*Institut de Ciència de Materials de Barcelona (ICMAB–CSIC), Campus de Bellaterra, 08193 Bellaterra, Barcelona, Spain*

[2]*Materials Research and Technology Department, Luxembourg Institute of Science and Technology, 5 avenue des Hauts-Fourneaux, L-4362 Esch/Alzette, Luxembourg*

(Received 17 July 2017; revised manuscript received 5 October 2017; published 6 November 2017)

By means of first-principles calculations, we investigate the thermal properties of silica as it evolves, under hydrostatic compression, from a stishovite phase into a $CaCl_2$-type structure. We compute the thermal conductivity tensor by solving the linearized Boltzmann transport equation iteratively in a wide temperature range, using for this the pressure-dependent harmonic and anharmonic interatomic couplings obtained from first principles. Most remarkably, we find that, at low temperatures, $SiO_2$ displays a large peak in the in-plane thermal conductivity and a highly anisotropic behavior close to the structural transformation. We trace back the origin of these features by analyzing the phonon contributions to the conductivity. We discuss the implications of our results in the general context of continuous structural transformations in solids, as well as the potential geological interest of our results for silica.

DOI: 10.1103/PhysRevB.96.195201

## I. INTRODUCTION

The thermal properties of solids and nanostructures are attracting a growing interest, both from the fundamental standpoint and for application-driven research. The quest for low thermal conductivity materials, for instance, is one of the main challenges in the development of efficient thermoelectric devices [1], while materials with a large thermal conductivity could help overcome the problem of heat dissipation at the nanoscale, which has become one of the major hitches for nanoscaling electronic devices [2,3]. The thermal properties of an insulating solid are governed by its lattice thermal conductivity. This physical property is determined by the lattice vibrational modes (phonons) and by the scattering processes they encounter. At structural phase transitions, which are driven by soft phonons, the lattice thermal conductivity is expected to be strongly modified, since the soft mode will experience a frequency and group velocity shift which will in turn modify the allowed phonon scattering processes in the system.

In this article we investigate the thermal properties of $SiO_2$ close to a structural phase transition. Some theoretical works have already calculated the thermal properties from first principles for a handful of oxides such as ferroelectric $PbTiO_3$ [4], MgO [5–7], and $MgSiO_3$ [8,9], but none of them was studied close to a structural phase transition. Transitional effects were addressed in Refs. [10,11] for PbTe-based ferroelectrics.

Silicon dioxide, also known as silica, is not only the most abundant compound on Earth [12], the Moon [13], and the terrestrial planets [12,14], but is also at the heart of modern day electronic devices and is widely used as a substrate in thin film growth. The phase diagram of $SiO_2$ is very rich, with a wide variety of silica polymorphs such as $\alpha$-quartz, $\beta$-quartz, cristobalite, tridymite, or coesite. In these phases Si shows a tetrahedral coordination with the surrounding O atoms. At high pressures (of the order of gigapascals) the coordination of silicon in $SiO_2$ becomes octahedral, giving rise to the stishovite phase, the $CaCl_2$-type phase, or the $\alpha$-$PbO_2$-type phase at even higher pressures (of the order of 100 GPa). In particular, the pressure induced phase transition from the stishovite to the $CaCl_2$-type phase is considered as a paradigmatic pseudoproper ferroelastic phase transition. While the atomic structure [15,16], phonon band structure [17–21], electronic structure [22–24], and thermodynamic potentials describing the structural phase transition [17,25–27] have been widely studied, both experimentally and theoretically, no previous work has addressed the thermal properties of the stishovite or the $CaCl_2$-type phases. In this work we calculate the thermal properties of the stishovite and $CaCl_2$-type high pressure phases of silica as a function of temperature and pressure from first principles.

## II. COMPUTATIONAL METHODS

### A. Density functional calculations of the interatomic force constants

We performed first-principles electronic structure calculations within density functional theory (DFT), using the Vienna *ab initio* simulation package [28,29] (VASP) along with the Perdew-Burke-Ernzerhof (PBE) [30] implementation of the generalized gradient approximation (GGA) for the exchange-correlation functional. We employed a plane wave basis set with a 500 eV kinetic energy cutoff with the projector augmented-wave method [31,32]. For the ground state calculations we considered the primitive cells of the stishovite and the $CaCl_2$-type phases (see Fig. 1) and carefully optimized the lattice vectors and the atomic position until the residual stress and the forces were smaller than $10^{-2}$ kbar and $10^{-6}$ eV/Å, respectively. The Brillouin zone (BZ) was sampled with a converged $4 \times 4 \times 6$ Monkhorst-Pack [33] grid of **k** points. Hydrostatic pressure was applied by varying the lattice vectors as described below, and allowing the atomic coordinates to relax.

We employed the direct supercell approach to obtain the phonon band structures. In this approach the second-order interatomic force constants (IFCs) are computed directly by considering supercells of the corresponding primitive cell with small enough (0.01 Å) atomic displacements. We employed the PHONOPY software [34] to generate the minimal set of supercells required to obtain the IFCs, while VASP was used to compute the Hellmann-Feynman forces in these cells. The

 

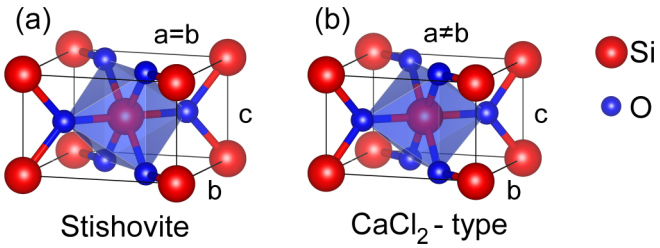


FIG. 1. Unit cell of $SiO_2$ in the stishovite phase (a) and the $CaCl_2$-type phase (b). Si (O) atoms are shown in red (blue). The stishovite phase is a tetragonal crystal while the $CaCl_2$-type phase is orthorhombic. Note that the oxygen octahedron (highlighted in blue) is tilted about the $c$ axis in the $CaCl_2$-type phase.

long-range corrections to the potential were included to correctly address for dipole-dipole interactions arising from longitudinal optic (LO) vibrational modes of the crystal. The supercells with atomic displacements employed to calculate the third-order IFCs, which account for the three-phonon scattering processes, were generated using THIRDORDER.PY [35]. We employed $3 \times 3 \times 4$ supercells for computing both the second- and third-order IFCs at each pressure, since we found that the subsequent lattice thermal conductivity is well converged when compared to the results obtained for $2 \times 2 \times 3$ supercells.

### B. Solution of the Boltzmann transport equation

The second- and third-order IFCs obtained from the DFT calculations were used to solve the linearized Boltzmann transport equation (BTE):

$$\boldsymbol{v}_\lambda \cdot \nabla T \frac{\partial n_\lambda^0}{\partial T} = \left.\frac{dn_\lambda}{dt}\right|_{\text{scatt.}}, \tag{1}$$

where $n_\lambda^0$ and $n_\lambda$ are the phonon distribution at and out of equilibrium, respectively, $\boldsymbol{v}_\lambda$ is the group velocity, and $dn_\lambda/dt|_{\text{scatt.}}$ is the rate of change in the phonon distribution as a result of phonon-phonon scattering. We can assume the difference between $n_\lambda$ and $n_\lambda^0$ to be of the form

$$n_\lambda = n_\lambda^0 - \boldsymbol{F}_\lambda \cdot \nabla T \partial n_\lambda^0 / \partial T. \tag{2}$$

Then, the linearized BTE can be rewritten in the following way [35]:

$$\boldsymbol{F}_\lambda = \tau_\lambda^0 (\boldsymbol{v}_\lambda + \boldsymbol{\Delta}_\lambda), \tag{3}$$

where $\boldsymbol{F}_\lambda$ is the generalized mean free path, $\tau_\lambda^0$ is the relaxation time of mode $\lambda$ in the relaxation time approximation (RTA), and $\boldsymbol{\Delta}_\lambda$ gives the deviation of the solution from the RTA. By taking into account only isotopic and anharmonic phonon scattering processes, we can write $\tau_\lambda^0$ as

$$\frac{1}{\tau_\lambda^0} = \Gamma_\lambda = \Gamma_\lambda^{\text{isot}} + \Gamma_\lambda^{\text{anh}}, \tag{4}$$

where the total scattering rate of mode $\lambda$, $\Gamma_\lambda$, is the sum of the isotopic scattering rate $\Gamma_\lambda^{\text{isot}}$ and the anharmonic scattering rate $\Gamma_\lambda^{\text{anh}}$. Scattering caused by isotopic disorder depends on the mass variance of the elements in the compound and was included through the model due to Tamura [36], for which we employed the natural abundances of Si and O (see Table I) [37]. Three-phonon scattering processes were included to account for the anharmonic scattering, which is computed directly from the third-order IFCs obtained from the DFT calculations. Higher order scattering processes were neglected, since they are expected to be important only at very high temperatures [38].

TABLE I. Stable isotopes of Si and O and their relative naturally occurring abundances [37].

| Isot. | Abund. (%) | Isot. | Abund. (%) |
|---|---|---|---|
| $^{28}$Si | 92.23 | $^{16}$O | 99.76 |
| $^{29}$Si | 4.67 | $^{17}$O | 0.038 |
| $^{30}$Si | 3.10 | $^{18}$O | 0.2 |

The BTE in the form given in Eq. (3) is solved iteratively [39] in a parameter-free approach as implemented in the SHENGBTE code [35] to obtain the lattice thermal conductivity tensor

$$\kappa_\ell^{\alpha\beta} = \frac{1}{k_B T^2 \Omega N} \sum_\lambda n^0 (n^0 + 1) (\hbar\omega_\lambda)^2 v_{\alpha,\lambda} F_{\beta,\lambda}, \tag{5}$$

where $\alpha$ and $\beta$ are the three coordinate directions $x$, $y$, and $z$; and $k_B$, $T$, $\Omega$, and $N$ are the Boltzmann constant, the temperature, the volume of the unit cell, and the number of $\mathbf{q}$ points in the integral over the BZ, respectively. The sum runs over all the phonon modes $\lambda$, $\hbar$ is the reduced Planck constant, and $\omega_\lambda$ is the phonon frequency.

For the first iteration step $\boldsymbol{\Delta}_\lambda$ is set to zero, which is tantamount to starting the iterative procedure from the RTA solution. The solution is considered to be converged when the relative change in all the components of the thermal conductivity tensor becomes smaller than $10^{-5}$.

### C. Convergence issues

The convergence tests of the relevant parameters of the electronic structure calculations—plane-wave energy cutoff, $\mathbf{k}$-point mesh—were carried out as usual. In the same way, we carefully checked the dependence of the IFCs on the supercell size, finding that a $3 \times 3 \times 4$ supercell yielded converged values.

Some convergence issues related to the numerical solution of the BTE must be addressed as well. The first one concerns the $\delta$ functions appearing in the energy conservation terms in the scattering rates, which are approximated by Gaussian functions for which the standard deviation is computed in a self-adaptive manner as implemented in the SHENGBTE code [35]. The locally adapted Gaussian standard deviation appearing in the computation of the scattering rates (both anharmonic and isotopic) was scaled by 0.1. This scaling was necessary because unscaled standard deviations prevented us from converging the solution of the BTE in a non-negligible subset of the targeted pressure-temperature values. However, we verified in a few cases where the unscaled calculation converged that the employed 0.1 scaling yielded minor quantitative differences in the thermal conductivity.

We also observed that solving the BTE in a too dense $\boldsymbol{q}$-point mesh could lead to an imaginary acoustic mode close to the critical pressure, because of inaccuracy of the Fourier

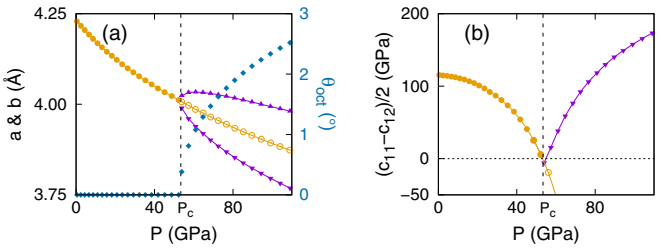


FIG. 2. (a) Lattice parameters $a$ and $b$ for $SiO_2$ as a function of pressure as obtained with DFT. Results for the stishovite phase are shown in orange (circles) while those for the $CaCl_2$-type phase are shown in purple (triangles). The rotation angle of the oxygen octahedron is shown with unconnected blue points. (b) Dressed shear modulus $\frac{(c_{11}-c_{12})}{2}$ as a function of pressure for the stishovite (orange) and $CaCl_2$-type (purple) phases. The shear modulus vanishes close to the phase transition.

interpolation in the calculation of the phonon bands. In order to avoid spurious effects due to such contributions we employed a slightly sparse **q**-point mesh ($6 \times 6 \times 6$) so that no imaginary frequencies are sampled close to the critical pressure around the $\Gamma$ point in the BZ integrations. Although the exact values of the conductivity are slightly underconverged with the **q**-point grid and hence not quantitatively accurate, particularly close to the lattice thermal conductivity peak at each temperature, we have checked that our main qualitative results remain valid with denser grids.

Finally, we stress that all the results discussed in this work have been obtained by solving the BTE iteratively. Nevertheless, we have found that the RTA results for the lattice thermal conductivity differ at most by 10% in the whole $(T, P)$ region we explored.

## III. RESULTS

### A. Phase transition under pressure

The crystal structure of the two silica polymorphs studied is shown in Fig. 1. The stishovite phase belongs to the tetragonal crystal family with space group $P4_2/mnm$, while the $CaCl_2$-type phase belongs to the orthorhombic crystal family with space group $Pnnm$. The latter differs from the former in a tilt of the oxygen octahedra surrounding the Si atoms and has lattice parameter $b \neq a$. We computed the relaxed lattice parameters and atomic positions of silica for pressures ranging from 0 to 100 GPa in both phases. In the stishovite phase we imposed $b = a$, while this restriction was lifted for the $CaCl_2$-type phase. The calculated $a$ and $b$ lattice parameters are shown in Fig. 2, along with the oxygen octahedra rotation angle. At the critical pressure, $a$ starts to differ from $b$, and the oxygen octahedra become tilted in the $CaCl_2$-type phase.

This phase transition is known to be driven by the softening of the optical $B_{1g}$ phonon mode in the BZ center, which corresponds precisely to a pure rotation of the oxygen octahedra. The critical pressure $P_c$ is taken as that for which the dressed shear modulus $(c_{11} - c_{12})/2$ (where the $c_{ij}$ is the $ij$ component of the stiffness tensor in Voigt notation) vanishes in the stishovite phase, i.e., the pressure at which the system shows no resistance to the shearing of the cell and the oxygen octahedra rotation. The computed shear modulus

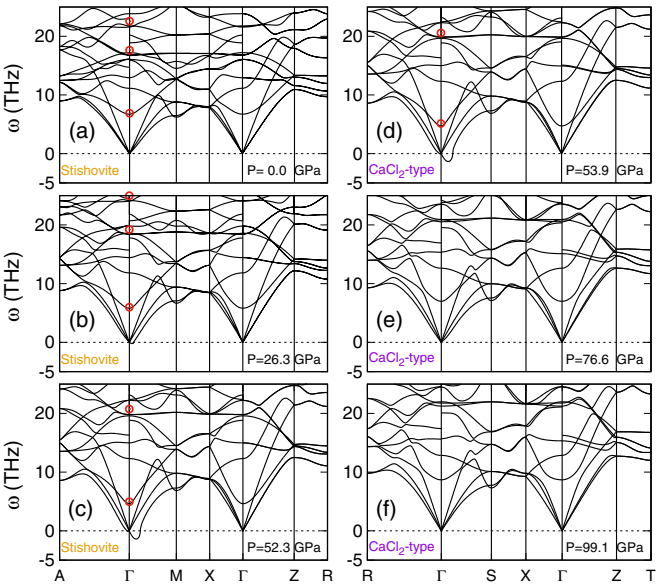


FIG. 3. (a)–(c) Phonon band structure for three representative pressures of the stishovite phase and (d)–(f) the $CaCl_2$-type phase. The modes have been computed for $P = 0$, 26.3, 52.3, 53.9, 76.6, and 99.1 GPa. Red circles correspond to experimental values for Raman-active modes (only available for pressures up to 60 GPa) taken from Ref. [43].

as a function of pressure is shown in Fig. 2(b). We obtain $P_c = 53.4$ GPa, in good agreement with previous calculations [17] and experiments [40]. This second-order phase transition is of the pseudoproper ferroelastic type, since the driving order parameter is not strain itself, but the strain emerging at the phase transition has the same symmetry as that order parameter [17,25,41].

Next, we compute the phonon band structure of silica in the stishovite and $CaCl_2$-type phases at different pressures. Some representative cases of both phases are shown in Fig. 3. We first note that some nondegenerate modes (such as the third and fourth optical modes) of the $CaCl_2$-type phase become degenerate in the stishovite phase due to the higher symmetry of silica in the tetragonal phase. Moreover, the phonon bands generally gain energy with increasing pressure, the only two exceptions being the lowest optical band around $\Gamma$ (associated with the $B_{1g}$ mode responsible for the structural phase transition), which softens close to $P = P_c$ and then gains energy together with the rest of the modes, and the lowest energy band in the high symmetry point $A$ ($S$) in the stishovite ($CaCl_2$-type) phase (see the video in the Supplemental Material [42]). For pressures between 25 and 70 GPa, one of the acoustic bands becomes imaginary in a small region of the BZ along the $\Gamma$-$M$ direction for the stishovite phase [17,21], and along the $\Gamma$-$S$ direction for the $CaCl_2$-type phase. This artifact is sometimes attributed in the literature to the finite supercell size employed in the calculations (see for instance Ref. [17]), but our tests for $SiO_2$ and other materials (e.g., $BaTiO_3$) seem to suggest that the problems persist even if considerably larger supercells are used. Instead, the appearance of imaginary acoustic modes close to the Brillouin zone center seems to be related to a systematic error due to the so-called Fourier

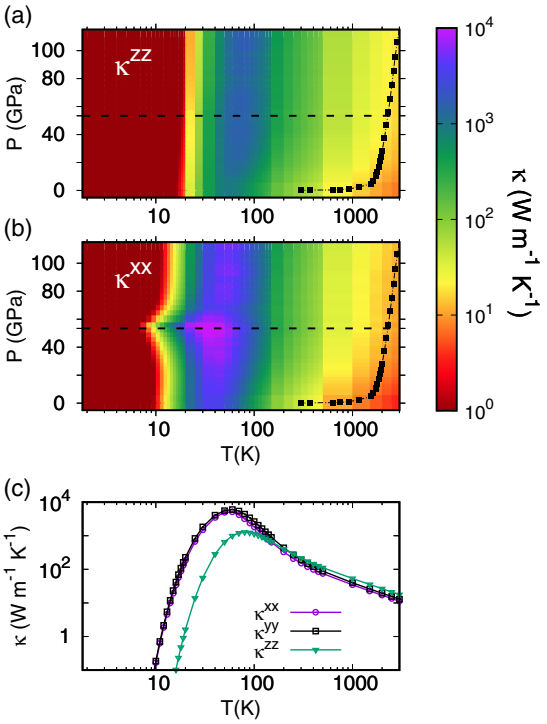


FIG. 4. Lattice thermal conductivity of $SiO_2$ for different pressures and temperatures (see color code on the right). The $zz$ component of the lattice thermal conductivity is shown in (a), and the $xx$ component in (b). The results for the stishovite phase are shown only for pressures below $P_c$, while the results for the $CaCl_2$-type phase are displayed above $P_c$. The $zz$ component shows a slight increase as pressure increases, but no special feature is seen at $P = P_c$. The $xx$ component is larger than the $zz$ one for $T < 200$ K, showing a huge enhancement around the critical pressure for temperatures below 40 K. Black squares show the average geotherm according to Dziewonski and Anderson's Earth model [44]. (c) Lattice thermal conductivity along the $P = 76.6$ GPa isobar. Purple circles, black squares, and green triangles correspond to the $xx$, $yy$, and $zz$ components, respectively.

interpolation of the dynamical matrix for noncommensurate **q** points. Naturally this issue becomes more obvious (even pathological) in regions where we have phonons with near-zero frequencies (as, e.g., in the center of the Brillouin zone), since in such cases a problem in the interpolation scheme will typically result in some frequencies becoming imaginary. Thus, the calculation of the integrals in reciprocal space appearing in the BTE must be done with care, avoiding the small region where this acoustic band becomes imaginary so that no unphysical results are obtained.

### B. Thermal conductivity

#### 1. Solution of the BTE in the $(T, P)$ space

We next solve the BTE for both silica phases for several values of temperature $T$ and pressure $P$. Figures 4(a) and 4(b) show the lattice thermal conductivity components $\kappa^{zz}$ and $\kappa^{xx}$, respectively. We find that the off-diagonal components are negligible in the whole $(T, P)$ space explored and that the $\kappa^{yy}$ component (not shown) is equal to the $\kappa^{xx}$ component in the stishovite phase due to symmetry. In the $CaCl_2$-type phase $\kappa^{yy}$

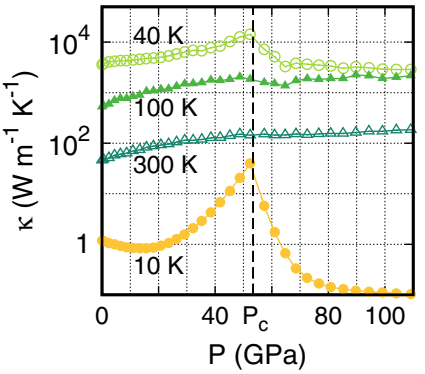


FIG. 5. Constant temperature profiles of $\kappa^{xx}$ as a function of pressure, for $T = 10$ K (filled circles), $T = 40$ K (empty circles), $T = 100$ K (filled triangles), and $T = 300$ K (empty triangles).

shows a similar behavior to $\kappa^{xx}$. For pressures below (above) the critical pressure we only show the results for the stishovite ($CaCl_2$-type phase), i.e., only the results for the stable phase at each pressure are shown. We first note that both components are substantially different in most of the $(T, P)$ space. More importantly, we find an astonishingly large peak in $\kappa^{xx}$ close to the critical pressure at both sides of the critical line for temperatures between 8 and 70 K.

In Fig. 4(c) we show the lattice thermal conductivity for the $P = 76.6$ GPa isobar. We find the characteristic trend of the lattice thermal conductivity curves for bulk systems. At low temperatures $\kappa$ increases with $T$ until it reaches a maximum, after which the conductivity decreases more slowly. We also note that $\kappa^{xx}$ is almost equal to $\kappa^{yy}$ in the whole temperature range, while $\kappa^{zz}$ is smaller below $T = 200$ K. Thus, the thermal response of silica is clearly anisotropic in general.

In Fig. 5 we show $\kappa^{xx}$ profiles for different isotherms. The lattice thermal conductivity close to $P = P_c$ increases up to 2 orders of magnitude for low temperatures (see the $T = 10$ K line in Fig. 5), and about 1 order of magnitude for medium temperatures (see the 40 K isotherm in the same figure). At higher temperatures, at which the scattering is dominated by anharmonic processes, the peak is smoothed out until it disappears (see the 100 and 300 K isotherms). This suggests that the peak stems from a shift in the dominant scattering processes, from isotopic to anharmonic phonon-phonon, as temperature increases (recall that we are calculating the bulk lattice thermal conductivity, thus ignoring boundary scattering processes). This can be confirmed, for example, by recomputing the thermal conductivity maps $\kappa(T, P)$ with no anharmonic scattering. Since isotopic scattering is dominant at low temperatures, we obtained almost identical results for $T < 100$ K, while at each pressure $\kappa(T)$ saturates to a constant value for $T \gtrsim 150$ K.

#### 2. Origin of the peak around the critical pressure

In order to trace the origin of the notorious peak in the in-plane thermal conductivity, we analyze the contribution to $\kappa^{xx}$ of each mode in each of the sampled points in the BZ. The individual contributions of all the modes included in our BZ integrations at different representative temperatures and pressures are depicted in Fig. 6. For each **q** point in the

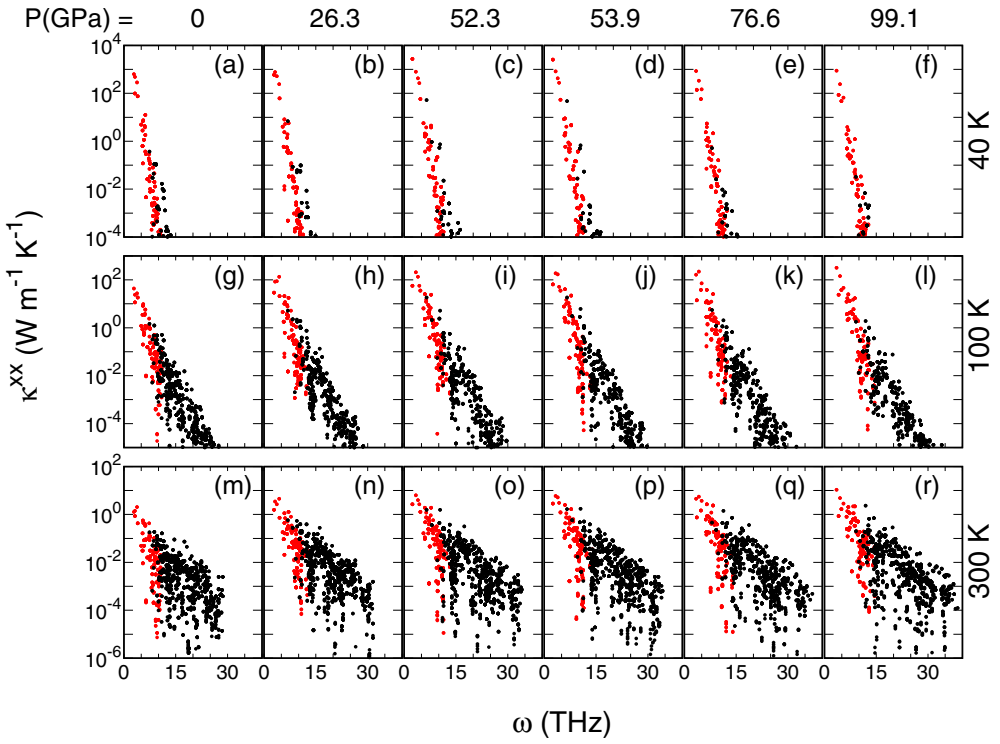


FIG. 6. Contribution to the total lattice thermal conductivity for each mode $\lambda$ ($\kappa_\lambda$). The first, second, and third rows correspond to calculations at $T = 40$, 100, and 300, K respectively. The columns from left to right correspond to $P = 0$, 26.3, 52.3, 53.9, 76.6, and 99.1 GPa, where the results are shown only for the stable phase at each pressure. Close to the critical pressure, a few acoustic modes are responsible for the anomalously large value of $\kappa^{xx}$ at (c) and (d) $T = 40$ K. For (g)–(l) $T = 100$ K and (m)–(r) $T = 300$ K, there is no peak in $\kappa^{xx}$ at $P = P_c$ and the $\kappa_\lambda$ of the highest contributing modes increases monotonically with pressure. Red (black) dots correspond to acoustic (optical) modes.

irreducible BZ the contribution of the 18 modes is shown. At $T = 40$ K (upper row in the figure), we see that $\kappa^{xx}$ is strongly dominated by the contribution of a few low energy modes. Also, one (degenerate) mode contributes with up to $2.7 \times 10^3$ W m$^{-1}$ K$^{-1}$ for $P \approx P_c$ but is not so active at high or low pressures. For higher temperatures ($T = 100$ K and $T = 300$ K, second and third rows in Fig. 6, respectively), although the dominant contributions still correspond to low energy modes, optical phonons start to play an increasingly important role in the total thermal conductivity. Furthermore, the general trend is a monotonic increase of the individual contributions with increasing pressure. In this way we can attribute the peak in the in-plane lattice thermal conductivity at low temperatures to the enhancement of the contribution of particular low energy acoustic modes.

We now analyze the evolution of the individual contributions $\kappa_\lambda^{xx}$ with pressure. The results for two representative temperatures (10 and 300 K) are shown in Fig. 7. The total $\kappa^{xx}$ is also presented with black filled circles for comparison. On the one hand, at $T = 10$ K thermal transport is dominated by essentially one mode—purple squares in Fig. 7, mode (I)—for pressures between 30 and 60 GPa (see that the total $\kappa^{xx}$ is almost equal to the contribution of this mode in this pressure range). The aforementioned mode is a low energy acoustic phonon with wave vector $\boldsymbol{q} = (1/6,1/6,0)$ in reciprocal vector units, which is representative of an entire region of low energy modes close to the BZ center. Away from this pressure window, the contribution of another acoustic mode—mode (II)—with $\boldsymbol{q} = (1/3,0,0)$ in reciprocal vector units (green squares) becomes larger than that of mode (I), hence dominating the thermal conductivity at low and high pressures. The contribution of the next highest contributing

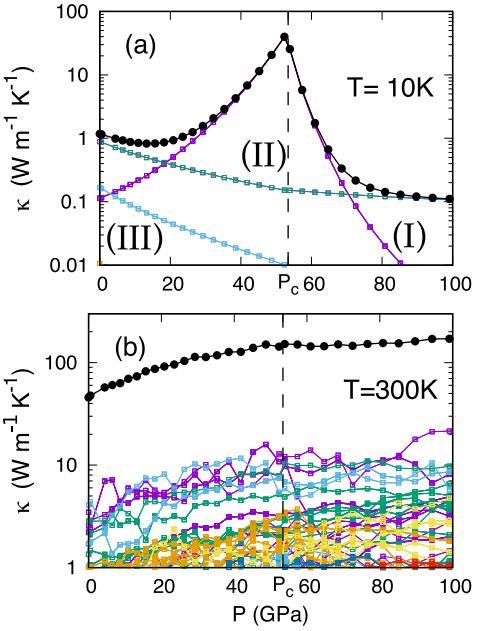


FIG. 7. Contribution to $\kappa^{xx}$ as a function of pressure of different modes for (a) $T = 10$ K and (b) $T = 300$ K. The total thermal conductivity at each temperature is shown in black circles.

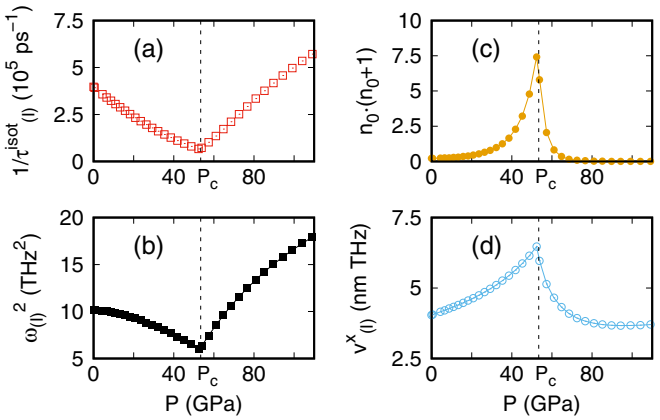


FIG. 8. (a)–(d) Evolution of isotopic scattering rate of mode (I), squared frequency of mode (I), $n_0(n_0+1)$ at $T = 10$ K for mode (I), and $x$ component of the group velocity of mode (I) with pressure, respectively. The critical pressure $P_c$ is indicated with a vertical dashed line as a guide to the eye in all cases.

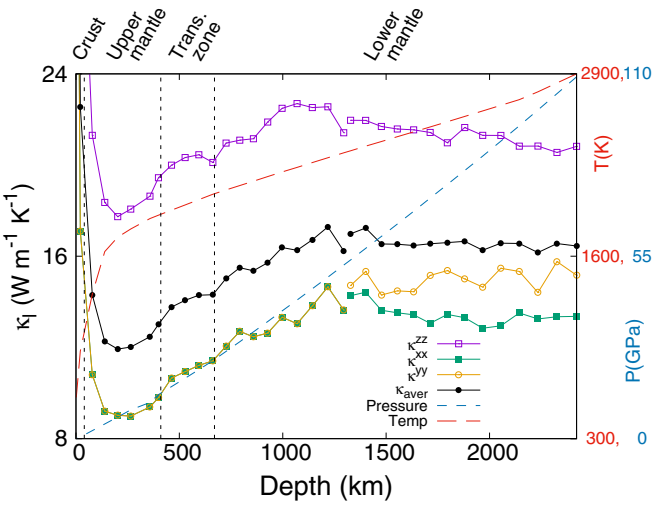


FIG. 9. Lattice thermal conductivity of silica in the stishovite and $CaCl_2$-type phases along an average geotherm. The results for the stishovite ($CaCl_2$-type) phase are shown for $P < (>)P_c$, and the phase transition is marked by a discontinuity in the lattice thermal conductivity lines. Filled squares, empty circles, and empty squares correspond to the diagonal components $\kappa^{xx}$, $\kappa^{yy}$, and $\kappa^{zz}$, respectively, and the average lattice thermal conductivity $\kappa_{\text{aver}} = \frac{1}{3}(\kappa^{xx} + \kappa^{yy} + \kappa^{zz})$ is shown with filled circles (see legend). The average estimated temperature (pressure) at each depth from the Earth's crust is shown with a long-(short-)dashed red (blue) line. There is a marked decrease in the three diagonal components of $\kappa$ close to $P = P_c$.

mode is about one order of magnitude smaller, thus thermal transport in silica close to the phase transition is strongly governed by the behavior of the acoustic phonons represented by mode (I). On the other hand, at $T = 300$ K many modes give contributions in the range of 1 to 10 $\text{W m}^{-1}\text{K}^{-1}$. The total $\kappa^{xx}$ is thus the addition of many contributions of similar magnitude, and no particular mode dominates the thermal transport properties of $SiO_2$ in the studied pressure range. Moreover, there is only a minor dip in the total thermal conductivity close to the critical pressure, and this feature cannot be attributed to an individual mode. Although the overall thermal conductivity increases almost monotonically with pressure, not all of the highly contributing modes follow this behavior.

With the aim of acquiring some deeper insight of the origin of the peak, we now analyze the different factors that determine the contribution of mode (I) and its evolution with pressure. Figure 8 shows the evolution with pressure of the main different factors involved in $\kappa^{xx}_{(\text{I})}$, namely the isotopic scattering rate, the square of the frequency, the product of populations $n^0_{(\text{I})}(n^0_{(\text{I})}+1)$, and the group velocity [see Eq. (5)]. While the term $\omega^2_{(\text{I})}$ decreases by a factor of 1.67 at the critical pressure (with respect to $P = 0$), the remaining pressure dependent factors increase as the pressure approaches $P_c$. In fact, a decreasing $\omega^2_\lambda$ is always overcompensated by the growth of $n^0_\lambda(n^0_\lambda+1)$, i.e., the softening of a phonon band results in a larger contribution to the thermal conductivity (not taking into account the possible changes in the relaxation times). The largest ratio for mode (I) is precisely that of the phonon population product $n^0_\lambda(n^0_\lambda+1)$, which accounts for a factor of 33.5 in the enhancement close to the critical pressure. The isotopic scattering rate (which at low temperatures is much larger than the anharmonic scattering rate) decreases by a factor of 6, increasing the contribution of mode (I) to the thermal conductivity by the same factor and being the second largest ratio. The decrease in the unit cell volume and the increase in group velocity close to $P_c$ contribute to the total ratio with factors of 1.1 and 2.6, respectively. The total enhancement factor is of 338.4.

### 3. *Thermal conductivity of* $SiO_2$ *along the geotherm*

The thermal conductivity of the Earth's mantle determines its convection mechanism and the heat budget of our planet [6]. Owing to the great interest of $SiO_2$ in the field of geophysics, we additionally computed the thermal conductivity tensor of silica along an average geotherm [44] from the Earth's crust up to depths of 2400 km, deep inside the lower mantle. The results are displayed in Fig. 9. We first note that for high temperatures the anisotropy is reversed, being $\kappa^{zz}$ larger than $\kappa^{xx}$ and $\kappa^{yy}$, as opposed to the results analyzed above for lower temperatures. In the stishovite phase, the three diagonal components increase approximately linearly with depth up to the critical pressure, while for the $CaCl_2$-type phase the thermal conductivity is roughly constant with depth. Nevertheless, a decrease in all the components is seen close to the phase transition, which is marked by a discontinuity in the lines in the figure. Interestingly, we note that in works by Murphy *et al.* on PbTe-based materials [10,11] a dip in the thermal conductivity of ferroelectric compounds was also predicted close to a structural phase transition.

## C. Discussion

The present work was partly motivated by our conjecture that $SiO_2$ should be a suitable model compound to investigate changes in thermal conductivity across a soft-mode-driven structural phase transition. Indeed, it seemed to us that $SiO_2$'s transformation between the stishovite and $CaCl_2$-type structures might be representative of other soft-mode ferroelastic (and ferroelectric) transitions, with the advantage that

the transition-controlling parameter (pressure, as opposed to temperature) is trivial to handle in a first-principles simulation. Hence, let us briefly discuss the generality of our findings for $SiO_2$, and whether our initial conjecture was correct.

Most importantly, our simulations predict that $SiO_2$ will display some strong changes in its low-temperature thermal conductivity around the transition pressure. Interestingly, such features are not directly related with the optical soft mode itself, which is the primary order parameter for the transformation but has a negligible impact in $\kappa$. Instead, they can be traced back to the accompanying softening of an acoustic band, an effect that is specific to the peculiar pseudoproper ferroelastic character of the investigated transition in $SiO_2$. Hence, this suggests that enhancements of the low-temperature conductivity, as those we observed in $SiO_2$, can be expected to occur at ferroelastic transitions involving a significant softening of the acoustic bands. Our results also suggest that, in contrast, other soft mode transformations as, e.g., ferroelectric or antiferrodistortive transitions in which only optical bands soften, will in general not present such marked effects in the thermal conductivity.

Additionally, our results show that, in $SiO_2$, significant changes in the lattice thermal conductivity are restricted to relatively low temperatures. More precisely, we find that, while the softening of the key acoustic band causes a large increase in its population at low temperatures [Fig. 8(c)], the relative population change is small at higher values of $T$; as a result, the effect in the conductivity at higher temperatures is modest as well. Naturally we do not know whether, in other materials, phonon frequencies and populations will control the variations of $\kappa$ to the same extent that we find they do in $SiO_2$. Yet, it is clear that, unlike the material-specific scattering rates or group velocities in Eq. (5), temperature-dependent populations are governed by universal laws. Therefore, the softening of a low frequency mode (either optical or acoustic) will in general enhance the low temperature thermal conductivity.

Nevertheless, let us note that, at higher temperatures, other factors can play a more dominant role. For example, as shown in Refs. [10,11], when three-phonon scattering becomes dominant, a mode softening can open (close) phonon-phonon scattering channels, leading to significant reductions (enhancements) of the thermal conductivity.

## IV. CONCLUSIONS

By means of state-of-the-art calculations, we have characterized the stishovite and $CaCl_2$-type high pressure phases of silica and computed a thermal conductivity map $\kappa(T,P)$ for a large number of points in the $(T,P)$ space. We found that, for pressures close to the phase transition, a large peak in the in-plane conductivity appears at both sides of the phase transition and at $T$ below 70 K. Moreover, this peak is not present in the out-of-plane conductivity, thus leading to a highly anisotropic thermal material. We have tracked down the origin of this unexpected peak, and found that it originates in the softening of an acoustic band that becomes highly populated close to the phase transition. We have discussed the general implications of our results, which suggest that lattice thermal conductivity effects associated to soft-mode transitions will be restricted to low temperatures and, thus, may not be promising for applications at ambient conditions. Finally, we have computed the thermal conductivity along an average geotherm for its possible applications in the field of geophysics, since $SiO_2$ is the most abundant compound in the Earth's mantle.

## ACKNOWLEDGMENTS

We acknowledge financial support by the Ministerio de Economía, Industria y Competitividad (MINECO) under Grant No. FEDER-MAT2013-40581-P and the Severo Ochoa Centres of Excellence Program under Grant No. SEV-2015-0496, and by the Generalitat de Catalunya under Grant No. 2014 SGR 301. We also acknowledge the financial support of the Luxembourg National Research Fund (Grant No. FNR/P12/4853155/Kreisel COFERMAT). We acknowledge the use of computational resources of CESGA, and the i2BASQUE academic network. Finally, we acknowledge Professor Robert T. Downs for pointing to Ref. [44].

[1] G. Mahan, APL Mater. **4**, 104806 (2016).
[2] G. Chen, *Nanoscale Energy Transport and Conversion: A Parallel Treatment of Electrons, Molecules, Phonons, and Photons* (Oxford University Press, Oxford, 2005).
[3] T. Luo and G. Chen, Phys. Chem. Chem. Phys. **15**, 3389 (2013).
[4] A. Roy, Phys. Rev. B **93**, 100101 (2016).
[5] S. Stackhouse, L. Stixrude, and B. B. Karki, Phys. Rev. Lett. **104**, 208501 (2010).
[6] X. Tang and J. Dong, Proc. Natl. Acad. Sci. USA **107**, 4539 (2010).
[7] H. Dekura and T. Tsuchiya, Phys. Rev. B **95**, 184303 (2017).
[8] H. Dekura, T. Tsuchiya, and J. Tsuchiya, Phys. Rev. Lett. **110**, 025904 (2013).
[9] X. Tang, M. C. Ntam, J. Dong, E. S. G. Rainey, and A. Kavner, Geophys. Res. Lett. **41**, 2746 (2014).
[10] R. M. Murphy, E. D. Murray, S. Fahy, and I. Savić, Phys. Rev. B **93**, 104304 (2016).
[11] R. M. Murphy, E. D. Murray, S. Fahy, and I. Savić, Phys. Rev. B **95**, 144302 (2017).
[12] J. W. Morgan and E. Anders, Proc. Natl. Acad. Sci. USA **77**, 6973 (1980).
[13] O. Kuskov, Phys. Earth Planet. Inter. **102**, 239 (1997).
[14] R. Rieder, T. Economou, H. Wänke, A. Turkevich, J. Crisp, J. Brückner, G. Dreibus, and H. McSween, Science **278**, 1771 (1997).
[15] M. A. Spackman, R. J. Hill, and G. V. Gibbs, Phys. Chem. Miner. **14**, 139 (1987).
[16] D. M. Teter, R. J. Hemley, G. Kresse, and J. Hafner, Phys. Rev. Lett. **80**, 2145 (1998).
[17] A. Togo, F. Oba, and I. Tanaka, Phys. Rev. B **78**, 134106 (2008).

[18] Y. Tsuchida and T. Yagi, Nature (London) **340**, 217 (1989).
[19] R. E. Cohen, *High-pressure Research: Application to Earth and Planetary Sciences* (American Geophysical Union, Washington, DC, 1993), pp. 425–431.
[20] A. R. Oganov, M. J. Gillan, and G. D. Price, Phys. Rev. B **71**, 064104 (2005).
[21] T. Tsuchiya, R. Caracas, and J. Tsuchiya, Geophys. Res. Lett. **31**, L11610 (2004).
[22] J. R. Alvarez and P. Rez, Solid State Commun. **108**, 37 (1998).
[23] D. Li, G. M. Bancroft, M. Kasrai, M. E. Fleet, R. A. Secco, X. H. Feng, K. H. Tan, and B. X. Yang, Am. Mineral. **79**, 622 (1994).
[24] A. Soldatov, M. Kasrai, and G. Bancroft, Solid State Commun. **115**, 687 (2000).
[25] M. A. Carpenter, R. J. Hemley, and H.-k. Mao, J. Geophys. Res.: Solid Earth **105**, 10807 (2000).
[26] M. A. Carpenter, Am. Mineral. **91**, 229 (2006).
[27] D. Andrault, G. Fiquet, F. Guyot, and M. Hanfland, Science **282**, 720 (1998).
[28] G. Kresse and J. Hafner, Phys. Rev. B **48**, 13115 (1993).
[29] G. Kresse and J. Furthmüller, Comput. Mater. Sci. **6**, 15 (1996).
[30] J. P. Perdew, K. Burke, and M. Ernzerhof, Phys. Rev. Lett. **77**, 3865 (1996).
[31] P. E. Blöchl, Phys. Rev. B **50**, 17953 (1994).
[32] G. Kresse and D. Joubert, Phys. Rev. B **59**, 1758 (1999).
[33] H. J. Monkhorst and J. D. Pack, Phys. Rev. B **13**, 5188 (1976).
[34] A. Togo and I. Tanaka, Scr. Mater. **108**, 1 (2015).
[35] W. Li, J. Carrete, N. A. Katcho, and N. Mingo, Comput. Phys. Commun. **185**, 1747 (2014).
[36] S.-I. Tamura, Phys. Rev. B **27**, 858 (1983).
[37] R. C. Weast, M. J. Astle, W. H. Beyer *et al.*, *CRC Handbook of Chemistry and Physics* (CRC, Boca Raton, FL, 1988).
[38] I. Pomeranchuk, Phys. Rev. **60**, 820 (1941).
[39] M. Omini and A. Sparavigna, Physica B (Amsterdam) **212**, 101 (1995).
[40] K. J. Kingma, R. E. Cohen, R. J. Hemley, and H.-k. Mao, Nature (London) **374**, 243 (1995).
[41] V. Wadhawan, *Introduction to Ferroic Materials* (CRC, Boca Raton, FL, 2000).
[42] See Supplemental Material at http://link.aps.org/supplemental/10.1103/PhysRevB.96.195201 for a video of the phonon band structure evolution of $SiO_2$ with pressure .
[43] D. L. Heinz, Nature (London) **374**, 216 (1995).
[44] A. M. Dziewonski and D. L. Anderson, Phys. Earth Planet. Inter. **25**, 297 (1981).